



**HAL**  
open science

## Evaporation process in porous silicon: cavitation vs pore-blocking

M Bossert, A Grosman, I Trimaille, F Souris, V Doebele, A Benoit-Gonin, Laurent Cagnon, P Spathis, Pierre-Etienne E Wolf, E Rolley

### ► To cite this version:

M Bossert, A Grosman, I Trimaille, F Souris, V Doebele, et al.. Evaporation process in porous silicon: cavitation vs pore-blocking. *Langmuir*, 2021, 37 (49), pp.14419-14428. 10.1021/acs.langmuir.1c02397 . hal-03394817

**HAL Id: hal-03394817**

**<https://hal.science/hal-03394817v1>**

Submitted on 22 Oct 2021

**HAL** is a multi-disciplinary open access archive for the deposit and dissemination of scientific research documents, whether they are published or not. The documents may come from teaching and research institutions in France or abroad, or from public or private research centers.

L'archive ouverte pluridisciplinaire **HAL**, est destinée au dépôt et à la diffusion de documents scientifiques de niveau recherche, publiés ou non, émanant des établissements d'enseignement et de recherche français ou étrangers, des laboratoires publics ou privés.

# Evaporation process in porous silicon: cavitation *vs* pore-blocking

M. Bossert, A. Grosman, I. Trimaille,<sup>1</sup> F. Souris, V. Doebele,  
A. Benoit-Gonin, L. Cagnon, P. Spathis, P.E. Wolf,<sup>2</sup> and E. Rolley<sup>3,\*</sup>

<sup>1</sup>*Sorbonne Université, CNRS, Institut des NanoSciences de Paris, INSP, F-75005 Paris, France*

<sup>2</sup>*Université Grenoble Alpes, CNRS, Institut Néel, F-38042 Grenoble, France*

<sup>3</sup>*Laboratoire de Physique de l'École Normale Supérieure, ENS, Université PSL,  
CNRS, Sorbonne Université, Université de Paris, F-75005 Paris, France*

We have measured sorption isotherms for helium and nitrogen in wide temperature ranges and for a series of porous silicon samples, both native samples and samples with reduced pore mouth so that the pores have an ink-bottle shape. Combining volumetric measurements and sensitive optical techniques, we show that, at high temperature, homogeneous cavitation is the relevant evaporation mechanism for all samples. At low temperature, the evaporation is controlled by meniscus recession, the detailed mechanism being dependent on the pore length and on the mouth reduction. Native samples and samples with ink-bottle pores shorter than one micrometer behave as an array of independent pores. In contrast, samples with long ink-bottle pores exhibit long-range correlations between pores. In this latter case, evaporation takes place by a collective percolation process and not by heterogeneous cavitation as previously proposed. The variety of evaporation mechanisms points to porous silicon being an anisotropic three dimensional pore network rather than an array of straight independent pores.

## INTRODUCTION

For a porous material where the pore transverse dimension is larger than a few tens of nanometers, it is usually assumed that cavitation in the liquid condensed in the pores is similar to cavitation in bulk liquid, provided that the liquid wets the pore walls. Evaporation by cavitation is expected to occur when the pores have a so-called ink-bottle shape, that is, if they are connected to the outer gas reservoir through small enough apertures [1–3]. Experiments when decreasing the gas pressure indeed show that evaporation takes place at a *well defined* pressure threshold [4, 5]. For large enough pores [5], this evaporation pressure is found to be consistent with the classical nucleation theory (CNT) for bulk liquid [6]. Using porous alumina as a model system, we have recently shown that the evaporation threshold is independent of the pore aperture diameter and consistent with CNT, providing a direct evidence for homogeneous cavitation [7].

Similar studies of the evaporation mechanism have been reported for porous silicon which, like porous alumina, is often described as an array of parallel independent pores [8]. As in the case of porous alumina, for small pore apertures, evaporation of hexane at room temperature also takes place at a well defined threshold, independent of the pore aperture [7]. However, this threshold is much larger than predicted by CNT. A similar discrepancy has been previously found using nitrogen at 77 K [9]. In both cases, it was argued that this discrepancy could result from heterogeneous cavitation. However, this hypothesis is contradictory with the fact that both fluids wet silicon. Moreover, it does not account for the surprising strong dependence of the evaporation threshold

on the pore length and diameter [7, 9].

Another classical explanation for a well defined evaporation threshold is that it follows from a percolation phenomenon in a disordered pore network [10]. This mechanism has been directly checked by optical measurements in Vycor [11–14]. However, this scenario requires interconnected pores. While this hypothesis seemed ruled out by measurements performed twenty years ago [15], a growing number of recent experiments (NMR diffusion measurements and X-ray tomography [16, 17]) suggest that there is indeed a large density of connections between neighboring pores. Similarly, while early investigation of adsorption isotherms [8] favored the picture of straight pores almost invariant along their axis, recent measurements of NMR diffusion [16, 17], permeability [16], and elastic constant anisotropy [18] suggest that constrictions are present along the pores.

In order to elucidate the true nature of the evaporation mechanism in porous silicon, we study in this paper its dependence on the temperature  $T$  and the pore length  $l$ , for both native silicon and silicon ink-bottles. We find that *homogeneous* cavitation is always dominant at high temperature, with a threshold consistent with the CNT prediction. As the temperature is decreased, an increasing fraction of the pores empties through meniscus recession from the sample's surface. Pore blocking is then sensitive to the pore network geometry. For native samples and short ink-bottles ( $l \lesssim 1 \mu\text{m}$ ), the recession occurs independently in the different pores, as expected for non-interconnected pores. In contrast, for long ink-bottle pores ( $l \gtrsim 5 \mu\text{m}$ ), we observe that evaporation presents long-range correlations between pores, directly evidencing the existence of interconnections. The steep evaporation event is then controlled by vapor percolation

in the disordered pore network.

This complex picture was built after systematic experiments. First, we used a sensitive optical method to measure sorption isotherms of nitrogen at a fixed temperature (77 K) for ink-bottle samples of increasing pore length  $l$  and evidence the role of  $l$ . Then, we measured evaporation isotherms over a broad range of temperatures. While the results in the short pore case pointed to the conventional picture of independent pores, this was not true for long pores. In order to elucidate the mechanisms of evaporation at play in this case, we combined the results of several experiments. In a first step, by comparing the evaporation of nitrogen and helium 4 (a perfectly wetting fluid), we ruled out the earlier hypothesis of heterogeneous cavitation in long pores. Second, by studying the temperature dependence of the evaporation pressure, both for native and ink-bottle samples, we evidenced a crossover between homogeneous cavitation at high temperature and meniscus recession at low temperature. Third, in the latter case, an optical interferometric technique [19] allowed us to reveal long-range spatial correlations between ink-bottle pores, and show the collective nature of evaporation by meniscus recession. Finally, putting together the results of these different experiments, we could propose a network geometry for thick porous silicon.

## MATERIALS AND METHODS

**Porous Silicon Samples.** Porous silicon samples are fabricated using the same procedure as in Ref.8, where the preparation process, the morphology and the physical properties of the samples are reported in detail. Samples are prepared by electro-etching of highly boron-doped (100) Si single crystal in hydrofluoric acid solution. One obtains parallel pores, perpendicular to the wafer surface, with a cross-section of polygonal shape. The pore size distribution is broad and depends on the concentration of the solution. Native samples used for synthesis of ink-bottles have two different porosities: for a nominal porosity of 70%, the pore transverse dimension  $d$  is  $12 < d < 40$  nm, with  $\langle d \rangle = 26$  nm. For a nominal porosity of 85%,  $d$  is  $23 < d < 80$  nm, with  $\langle d \rangle = 50$  nm. In addition, we also studied a 50% porosity native sample ( $7 < d < 19$  nm,  $\langle d \rangle = 13$  nm).

We use monolithic samples still attached to the underlying wafer. The lateral size is of the order of 1 cm. The thickness of the porous layer, hence the pore length  $l$ , is proportional to the etching time. In this work,  $l$  is varied from 1 to 40  $\mu\text{m}$ . Note that, in almost all earlier studies of adsorption in porous silicon,  $l$  was larger than 10  $\mu\text{m}$  [8, 15, 20–22]. The list of samples with their main characteristics is summarized in table I.

**Reduction of the pore mouth.** In order to observe

cavitation, the pores have to present an ink-bottle geometry. For most samples, the reduction of the pore mouth at the outer surface of the sample is obtained by multiple deposition of atomic layers of alumina (Atomic Layer Deposition). We used a ANRIC - AT400 reactor, mostly in continuous mode. In this case, trimethyl-aluminum and water exposition time is short so that the alumina layer is formed only at the pore mouth. Based on isotherms measurements, we empirically fixed the number of ALD cycles in such a way that the accessible porous volume is reduced, but only slightly. Most pores, except the ones with the smallest apertures, are then still accessible to the fluid. For the present purpose, we do not need to know the resulting size distribution of (reduced) pore mouth, but we stress that it is presumably as broad as the native distribution. Indeed, ALD is ideally a conformal process, so that the diameter distribution of apertures is simply the native one downshifted by twice the (uniform) alumina thickness.

Figure	Fluid	Porosity	$l(\mu\text{m})$	pore mouth reduction
1	N2	70%	1	20 ALD cycles
1	N2	70%	5	55 ALD cycles
1, 4, 6a, 7	N2	70%	20	55 ALD cycles
1	N2	70%	40	55 ALD cycles
2, 3	N2	85%	2	20 ALD cycles
5, 6b	He	70%	20	8 Al layers - 2 nm each [7]
8	C <sub>6</sub> H <sub>14</sub>	70%	20	8 Al layers - 2 nm each [7]
9	N2	70%	20	none
Sup. Mat.	N2	50%	20	none
10	N2	85%	20	60 to 160 ALD cycles

TABLE I. Samples used in the present work. The "short pore" behavior is observed for the two samples 70% - 1  $\mu\text{m}$  and 85% - 2  $\mu\text{m}$ . The reduction of pore mouth is obtained through ALD deposition as described in the text except for the 85% - 2  $\mu\text{m}$ . For this particular sample, the exposition time is of the order of 10 s, much larger than the one for the continuous mode (smaller than 1 s).

## Sorption Isotherms

*Nitrogen volumetric isotherms* - For samples with long pores, nitrogen sorption isotherms were performed over a large range of temperatures,  $64 \text{ K} < T < 116 \text{ K}$ . The isotherms are measured volumetrically using a commercial apparatus (HPVA II Micromeritics) equipped with 1000 Torr and 100 bar pressure transducers. The manifold at room temperature is connected to the cell containing the sample. The cell is cooled at low temperature by a homemade cryostat. We measure the admitted quantity as a function of pressure, up to the vapor saturation pressure, both with and without the sample for each temperature of interest. The difference between the two measurements yields the adsorbed amount. This procedure is required due to the large dead volume between the manifold and the cell. The associated uncertainty prevents us to study temperatures higher than 116 K, where the amount condensed in the sample is only 3% of

the total fluid amount (see typical isotherms in the Supporting Information). In the whole temperature range, the adsorbed quantity is computed taking into account the non-ideality of the gas phase through the compressibility factor [23, 24].

*Nitrogen optical isotherms* - The porous silicon layer being transparent above a wavelength  $\simeq 500$  nm, the condensed mass could be determined using white light interferometry (WLI) [19, 25] rather than volumetric measurements. The key advantage of the method is its better sensitivity, which enables measurement of thin samples with very small porous volumes. The porous layer is illuminated by a white light beam (500 to 900 nm). The interference between the beams reflected at both sides of the porous layer creates fringes in the spectrum of the reflected light. As the mean distance between pores is less than 100 nm, the porous layer appears as an homogeneous film (provided that the pore liquid content is statistically uniform), and the Fourier transform of the spectrum exhibits a single peak corresponding to the optical thickness  $L$  of the layer. Along the sorption isotherm, the shift  $\Delta L$  of this thickness is proportional to the adsorbed amount within a few percent. Optical sorption isotherms  $\Delta L = f(P/P_{\text{sat}})$  thus have a shape very similar to that of ordinary sorption isotherms obtained through volumetry [19]. This method is extremely sensitive almost up to the critical bulk point as, in contrast to volumetry, the interference does not depend on the contents of dead volumes outside the membrane. In practice, using a specially designed optical cryostat, it allows us to measure sorption isotherms for the thinnest porous layers (1  $\mu\text{m}$ ) with a very small porous volume (less than  $\sim 10^{-9}$   $\text{cm}^3$ ) up to 124 K and 30 bar.

*Helium volumetric isotherms* - Helium sorption isotherms were performed over a large range of temperatures,  $2.38 \text{ K} < T < 4.65 \text{ K}$ . The isotherms are obtained with a homemade setup using a continuous volumetric technique. The sample is placed in an annular copper cell inside a modified commercial  $^4\text{He}$  circulation cryostat. The cell is filled or emptied through a capillary line connected to a gas-handling manifold at room temperature. The pressure inside the cell is measured at room temperature using a separate capillary line, so as to suppress, for the used flow rates, the viscous pressure drop along the capillary. The cell temperature is regulated with a typical r.m.s. stability of 1 mK and measured using a Cernox<sup>TM</sup> thermometer calibrated against the saturated vapor pressure of helium. Condensation and evaporation isotherms are respectively obtained by connecting, through a voltage-controlled precision microvalve (Pfeifer EVR-116), the cell to a reservoir of pressurized gas at constant pressure or to a pump, and measuring the time evolution of the cell pressure  $P(t)$ . The helium mass inside the membrane can be retrieved once the total flow rate through the microvalve and the effective dead vol-

ume are known. In practice, as evaporation inside the membrane occurs over a narrow pressure range, the evaporation pressure is simply determined as the pressure for which the time derivative  $|\dot{P}(t)|$  is minimal (see Supporting Information).

**Determination of the diameters of constrictions and interconnections.** For evaporation by meniscus recession, the evaporation pressure for nitrogen and helium was converted into an effective pore diameter by assuming that recession takes place at equilibrium. To relate the equilibrium pressure to the pore diameter, we use the model developed by Saam and Cole for a cylindrical pore [26], which takes into account the van der Waals interaction between the fluid and the substrate. We assume that the interaction between those fluids and porous silicon is close to that with quartz, computed to be around 4400 and 1200  $\text{K} \cdot \text{\AA}^3$  respectively for  $\text{N}_2$  and  $^4\text{He}$  [27]. The calculated pore diameters are quite insensitive to the assumed interaction strength. Changing this interaction strength by a factor of 10 only modifies the calculated pore diameter by about 1 nm. Note that, since the pores in porous silicon have a polygonal shape, the calculated diameters should rather be considered as a typical transverse dimension (this also holds for the estimated diameter of connections between pores).

#### CNT prediction for the cavitation threshold.

From the measured isotherms, we deduce the vapor pressure at which evaporation takes place inside the sample, and compare this pressure with the Classical Nucleation Theory (CNT) prediction for bulk cavitation. Here, we sketch how we evaluate this CNT prediction.

According to CNT [6], the nucleation rate per unit volume is given by:

$$J = J_0 \exp(-E_b/k_B T) \quad (1)$$

where  $J_0$  is a prefactor. The energy barrier  $E_b$  for nucleating the critical bubble is:

$$E_b = \frac{16\pi}{3} \frac{\gamma^3}{(P_V - P_L)^2} \quad (2)$$

where  $\gamma$  is the surface tension,  $P_L$  the pressure of the metastable liquid phase, and  $P_V$  the pressure of the vapor inside the critical bubble. As the critical bubble is in (unstable) equilibrium with the surrounding liquid phase, the chemical potentials  $\mu_L$  and  $\mu_V$  are equal:

$$\mu_L(P_L) = \mu_V(P_V) \quad (3)$$

The vapor and liquid chemical potentials are respectively computed from the fugacity of the vapor [23, 24], and by assuming a constant compressibility of the liquid

(between saturation and  $P_L$ ). This allows us to compute  $E_b$  as a function of  $P_V$ , which coincides with the reservoir pressure, since this reservoir is at phase equilibrium with the liquid.

The cavitation pressure  $P_V^{\text{cav}}$  is then deduced from the value of  $E_b$  at cavitation, itself determined by the condition  $J(P_V^{\text{cav}})V\tau \simeq 1$ , where  $V$  is the volume of liquid (here the pore volume) and  $\tau$  the observation time, typically 100 s for the experiments using nitrogen.  $P_V^{\text{cav}}$  is thus set by the implicit equation:

$$E_b(P_V^{\text{cav}}) = \ln(J_0 V \tau) k_B T \quad (4)$$

The prefactor  $J_0$  depends on the dynamics of the critical bubble [6]. For nitrogen experiments, the dynamics is controlled by viscous dissipation [6, 28, 29] and we use the corresponding expression for  $J_0$ . In the middle of the experimental temperature range ( $T = 100$  K),  $J_0 \simeq 10^{38} \text{s}^{-1} \text{m}^{-3}$  and  $E_b \simeq 46 k_B T$ . For helium experiments,  $E_b$  lies in the range 40-45  $k_B T$ , depending on the estimation of  $J_0$  [6, 30]. For both fluids, because of the logarithmic dependence, the precise values of  $J_0$ ,  $\tau$ , and  $V$  have a small impact on the predicted value for  $P_V^{\text{cav}}$ .

## RESULTS

We first report on the experiments in porous silicon samples with alumina deposition : in the first subsections, it is implied that all samples have a reduced pore mouth. Only the last subsection is devoted to native samples.

### Impact of pore length on the shape of the isotherm

We have measured optical isotherms for several pore lengths and two porosities with  $\text{N}_2$  at 77 K. Figure 1 shows the measured isotherms for the samples of 70% porosity with pore lengths of 1, 5, 20 and 40  $\mu\text{m}$ .

For the 1  $\mu\text{m}$ -long pores (blue curve in Fig.1), evaporation takes place in two steps. Starting from the filled membrane, a progressive emptying is followed by a steep evaporation step at a pressure  $P_c \approx 0.49 P_{\text{sat}}$ . This "short pore" behaviour is also observed for the 2  $\mu\text{m}$ /85% porosity sample. As shown by the 77.8 K isotherm in Fig. 2, an evaporation step takes place at the same value of  $P_c$ . This pressure is very close to the value measured by Baidakov *et al.* in cavitation experiments on superheated bulk nitrogen [29]. This shows that, for short pores terminated by narrow enough apertures, evaporation takes place by cavitation. Moreover, for these pores whose mean diameter is a few tens of nanometers, no significant confinement

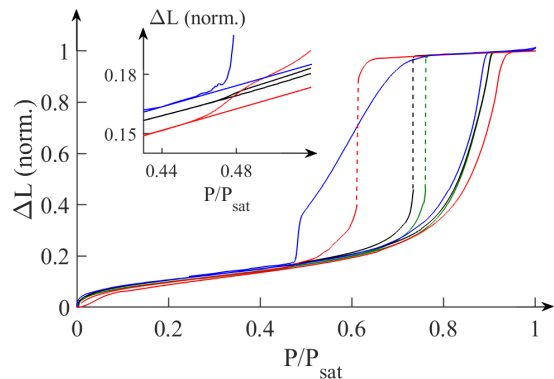


FIG. 1. Normalized nitrogen optical isotherms at 77.8 K for three porous silicon samples of 70% porosity. Blue:  $l = 1 \mu\text{m}$  - red:  $l = 5 \mu\text{m}$  - black:  $l = 20 \mu\text{m}$  - green:  $l = 40 \mu\text{m}$  (see Table I for the respective mouth reduction). The inset shows the secondary evaporation event around  $0.48 P_{\text{sat}}$  which we ascribe to homogeneous cavitation.

effect is observable, in agreement with earlier results on evaporation in cage-like porous silicas with large pores [5].

This "short pore" behaviour contrasts with that observed for longer pores in Fig.1 (5 to 40  $\mu\text{m}$ ). In this case, a sharp evaporation event directly occurs at a threshold  $P_p > P_c$  which depends on the pore length. Such a "long pore" behaviour is observed in all samples at 77 K, for pore lengths ranging from 4 to 60  $\mu\text{m}$  and porosities of 70 % and 85%. The general trend is that  $P_p$  increases with the length and mean diameter of the pores.  $P_p$  depends very weakly on the thickness of the alumina deposit – hence on the reduction of the pore mouth. Below  $P_p$ , the membrane contents slowly decreases down to around  $0.48 P_{\text{sat}}$ , very close to  $P_c$  for short pores. As shown by the inset of Fig.1, optical isotherms reveal a second evaporation event around this pressure, albeit with a much smaller amplitude than the first event.

### Short pores: changing the temperature

Further evidence that evaporation at  $P_c$  is due to cavitation can be obtained by studying the temperature evolution of "short pore" sorption isotherms. In Fig. 2, we show optical isotherms for a "short pore" sample (2  $\mu\text{m}$ /85%). The amplitude of the cavitation event, small at 77 K, increases with the temperature  $T$ . The corresponding cavitation pressure  $P_c(T)$  is compared to the CNT prediction in Fig. 3. The agreement is good at high temperature, confirming the cavitation nature of evaporation. At low temperature, the cavitation threshold is slightly higher than predicted. This result is in qualitative agreement with earlier measurements of cavitation in bulk superheated nitrogen [29] as well as in other fluids far below their critical point (hexane [7], heptane [31],

ethanol [31, 32], water [33]).

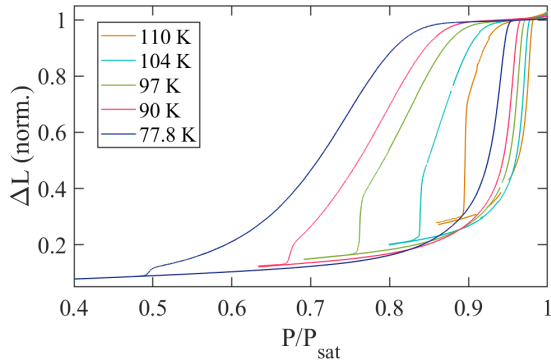


FIG. 2. Normalized nitrogen optical isotherms for a "short pore" sample  $2 \mu\text{m}$  thick (85 % porosity, 20 ALD cycles).

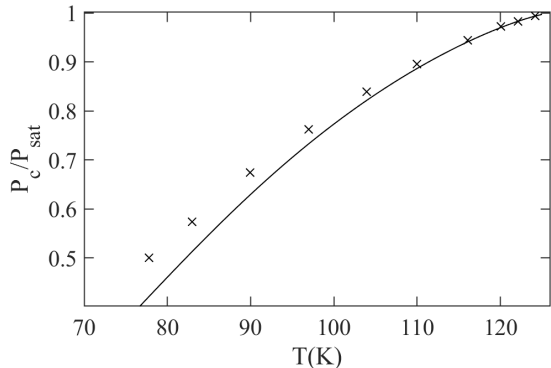


FIG. 3. Temperature dependence of the relative cavitation pressures ( $P_c/P_{\text{sat}}$ ) for a "short pore" sample ( $2 \mu\text{m}/85\%$  porosity/20 ALD cycles). The experimental points are represented by the crosses. The solid line represent the CNT predictions for  $\text{N}_2$ , with an energy barrier of  $46k_B T$ .

The temperature evolution of the isotherm shape shown by Fig. 2 is consistent with the large distribution of pore apertures. At 77 K, most pores have large enough apertures to empty through meniscus recession before reaching the metastability limit in the bulk of the pore, and cavitation only takes place in the narrowest pores with the narrowest apertures. As the temperature increases, the cavitation pressure increases faster than the equilibrium pressure in the apertures, and an increasing number of pores empty by cavitation. This accounts for the increase in relative height of the cavitation step. Above 120 K, all pores empty through cavitation.

### Long pores: changing the temperature

We now turn to the "long pore" samples. Here, we have used volumetric setups in order to measure the temperature dependence of the sorption isotherms.

Nitrogen isotherms are shown in figure 4 for a sample of porosity 70%, thickness  $20 \mu\text{m}$ , coated with 55 ALD cycles. At all temperatures, we observe that nitrogen mostly evaporates at a well defined threshold. Note that the sensitivity of the commercial apparatus is too low to detect a possible small secondary cavitation event similar to that detected at 77 K by WLI (inset of Fig 1).

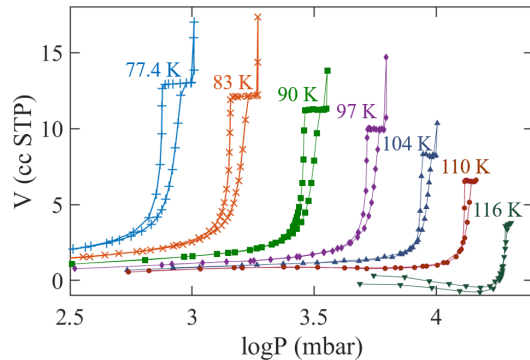


FIG. 4. Temperature dependence of nitrogen sorption isotherms for a porous silicon sample of porosity 70%, thickness  $20 \mu\text{m}$ , and 55 ALD cycles. The non-physical shape of the isotherm at 116 K at low pressure is an artefact due to the poor sensitivity at high temperature, but it remains easy to determine the pressure of the evaporation step.

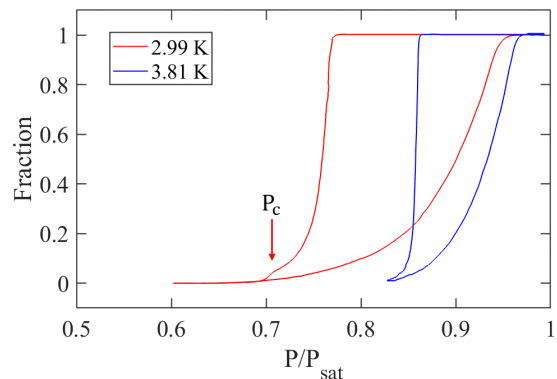


FIG. 5. Helium sorption hysteresis loops for a porous silicon sample of porosity 70%, thickness  $20 \mu\text{m}$ , with pore mouth reduced as described in the text. The vertical scale has been adjusted to be respectively 0 and 1 at the lower and upper closure points of the hysteresis loop. The two temperatures lie on both sides of the crossover temperature  $T^*$ . At the lower temperature, the secondary evaporation event at  $P_c$  is similar to that detected with nitrogen using WLI.

Similar experiments were performed with helium-4 using a different sample with the same 70% porosity and thickness  $20 \mu\text{m}$ . This sample had been previously used for the hexane experiments reported in Ref.7. In this case, instead of using ALD, the pore mouth was reduced by evaporating a 2 nm Al layer which is subsequently oxidized, this procedure being repeated 8 times [7]. As

illustrated by the hysteresis loops in Fig. 5, evaporation mostly takes place at a well defined threshold whatever the temperature (see Supporting Information for details). However, at low temperature, the continuous volumetric technique used in this case also reveals a small evaporation event at  $P_c$ . As discussed below, this event is similar to that detected with nitrogen using WLI, and corresponds to cavitation.

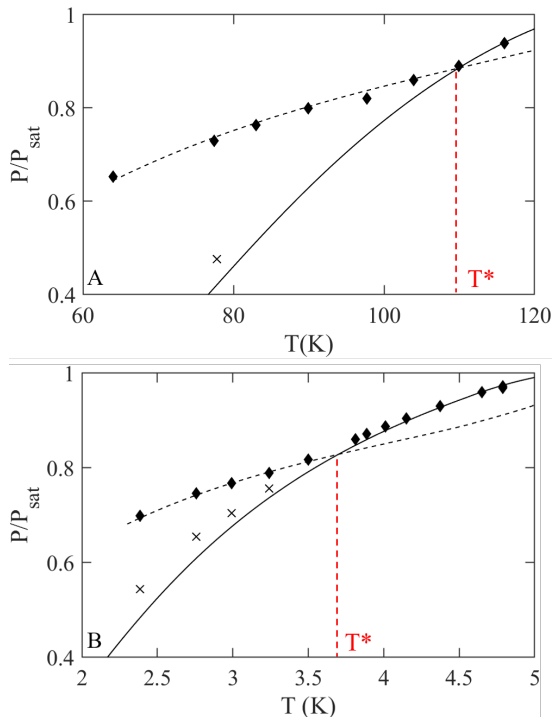


FIG. 6. Temperature dependence of the evaporation pressure ( $P/P_{\text{sat}}$ ) for  $\text{N}_2$  (A) and  $^4\text{He}$  (B) in 70% porosity and  $20 \mu\text{m}$  thick porous silicon samples with various alumina deposits. Diamonds correspond to the steep evaporation, while crosses correspond to the evaporation of a small fraction of the pores *via* homogeneous cavitation (the cross in A corresponds to the event shown in the inset of Fig 1). For both fluids, the solid lines represent the CNT prediction for a constant energy barrier of  $46k_B T$ , and the dashed lines are the theoretical curves for evaporation through recession of a liquid-vapor meniscus in a straight cylindrical pore of 9 nm diameter, calculated from Ref. [26, 27].  $T^*$  is the crossover temperature between the two evaporation processes.

Results for  $\text{N}_2$  and He are respectively summarized in Figs. 6 (a) and (b), which show the pressures of the main evaporation step (black diamonds) and of the secondary event (crosses). The full lines in Figs. 6(a) and (b) correspond to the CNT predictions for the cavitation pressure, using a constant energy barrier of  $46k_B T$ , and the dashed lines to the equilibrium pressure in a straight cylindrical pore 9-nm in diameter. In a similar way to an earlier study of evaporation in ordered large-cage mesoporous silicas [4], comparison of the experimental points to the theoretical lines demonstrates the existence of a

temperature crossover between two evaporation mechanisms. Above a temperature crossover  $T^*$ , evaporation mostly takes place at the same pressure  $P_c$  as in "short pore" samples, consistent with homogeneous cavitation. Below  $T^*$ , the pressure threshold  $P_p$  strongly deviates from the CNT curve. For both helium and nitrogen,  $P_p$  is found equal to the equilibrium pressure in 9-nm diameter cylindrical pores, suggesting that it is controlled by meniscus recession in such apertures. Nevertheless, the pressure of the secondary event is consistent with CNT, showing that a small fraction of the fluid still evaporates through cavitation.

### A closer look at evaporation in "long pore" samples

In order to shed light on the evaporation mechanism at play in "long pores" samples, we use an original approach, which consists in monitoring the pressure dependence of the FFT spectrum of the reflected light. An example is shown in Fig.7 for a sample with porosity 70% and thickness  $20 \mu\text{m}$ . On the saturation plateau (point A in the inset of Fig. 7), and at the end of the evaporation step (point C in the inset of Fig. 7), the Fourier transform of the reflected intensity versus optical wavelength shows a *single* peak at optical thicknesses corresponding respectively to a saturated or a nearly empty porous layer. If pores would evaporate independently, one would expect the peak to continuously shift between A and C on the evaporation branch. Indeed, the distance between pores being much smaller than the optical wavelength, the reflected light spectrum measures the average of the fluid density over many pores, which, since neighboring pores have uncorrelated diameters, should vary continuously during evaporation. Such a behaviour is indeed observed for "long pore" *native* samples at porosities of 70% and 85% (see Supporting Information). In contrast, the behaviour for "long pore" *ink-bottles* is strikingly different. As shown by Fig.7, the spectrum at point B in the inset of Fig. 7 is a linear combination of the two peaks above: during evaporation, the amplitude of the "saturated" peak ( $L_f$ ) decreases while that of the "empty" peak ( $L_e$ ) grows. This peak splitting, rather than the emergence of a single peak corresponding to an intermediate fluid content in the porous layer, means that evaporation is correlated over distances much larger than the pore spacing, directly evidencing the collective nature of evaporation between neighboring pores.

We have confirmed this long range correlation of evaporation in "long pore" samples by direct, high spatial resolution, optical imaging. Imaging the evaporation process is indeed possible using hexane at room temperature instead of nitrogen. In this case, a spatial resolution of  $1 \mu\text{m}$  can be reached because of the smaller distance between the sample and the imaging lens, compared to

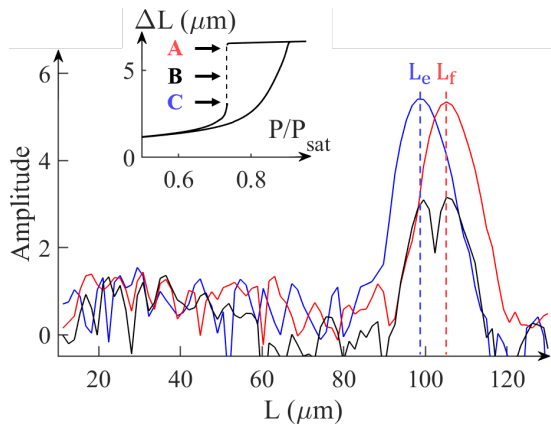


FIG. 7. Fourier transform of the reflected light spectrum during  $N_2$  evaporation at 77.8 K for a "long pore" sample (porosity 70%, thickness  $20 \mu\text{m}$  and 55 ALD layers). **A** saturated sample just before evaporation (dashed line), **B** during evaporation (red) and **C** at the end of evaporation (black solid line). Inset: corresponding optical isotherm with points **A**, **B**, **C**.

the low temperature setup, combined with the enhanced contrast between saturated and empty regions due to the larger optical index of hexane compared to nitrogen. Figure 8 shows a series of successive pictures taken during the main evaporation event for a "long pore sample". Evaporation clearly proceeds from a few spots through the emptying of large patches of neighbouring pores. The correlation length of the resulting pattern is of the order of  $10 \mu\text{m}$ , about 2 orders of magnitude larger than the mean distance between pores.

### Evaporation in native "long pore" samples

We now turn to *native* "long pore" samples, *i.e.* without pore mouth reduction. For such samples, isotherms (presented in Supporting Information) show a steep evaporation event at high temperature. At low temperature, desorption is not as steep and we define the evaporation pressure at mid-height of the evaporation step. The temperature dependence of the normalized evaporation pressure is shown in figure 9 for a 70% porosity sample  $20 \mu\text{m}$  thick. We find that the behavior of the native sample is similar to that of the same sample with alumina deposition (Fig. 6): at high temperature, evaporation occurs through cavitation while below a crossover temperature  $T^* \approx 114 \text{ K}$ , evaporation occurs through meniscus recession in an effective aperture of diameter  $D_{\text{eff}} = 10.9 \text{ nm}$ . This value is significantly larger than  $d_{\text{eff}} = 9 \text{ nm}$  found for the sample with alumina deposition.

This difference in effective diameters suggests that, at low temperature, evaporation by meniscus recession follows different paths in native samples and ink-bottle

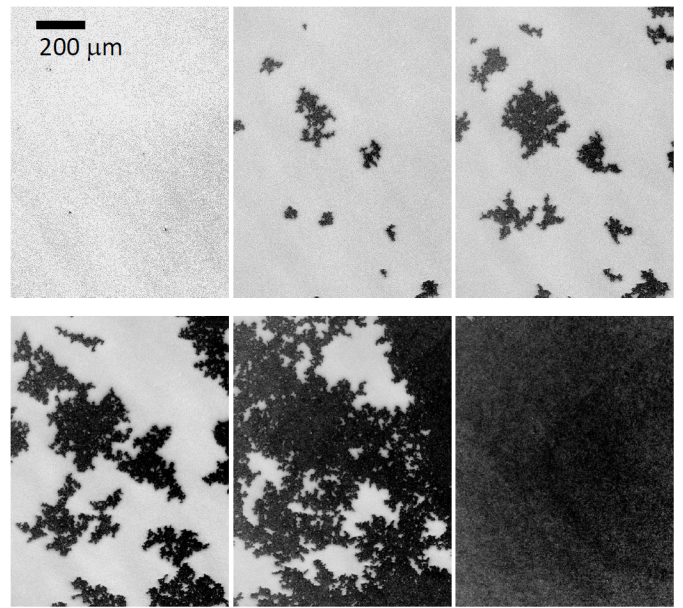


FIG. 8. Successive images of a "long pore" sample during the main evaporation event with hexane (same sample as the one used for  $^4\text{He}$  experiments,  $T = 18^\circ\text{C}$ ). Using the small difference (about 1%) of effective optical indices, hence reflectivities, between the filled and empty porous layer, contrast enhancing reveals the filled parts of the sample (bright) and the empty ones (dark). The pressure relative to  $P_{\text{sat}}$  is 0.58 in the middle of the evaporation step and changes by  $7 \cdot 10^{-4}$  from one image to the next.

samples. This is directly confirmed by the study of the reflected light spectrum for the native sample. In contrast to the ink-bottle samples, the Fourier transform of this spectrum does not reveal any peak splitting during evaporation (see Supporting Information). This means that native samples do not show any long-range correlation during evaporation.

For native 50% porosity samples, we have also measured the evaporation pressure as a function of the temperature and we find the same crossover from meniscus recession at low temperature to cavitation at high temperature (see Supporting Information). For 50% porosity, we find  $D_{\text{eff}} = 6.2 \text{ nm}$  and  $T^* = 97 \text{ K}$ . For native 85% porosity samples, we have only measured the evaporation pressure at 77 K, which gives  $D_{\text{eff}} = 18 \text{ nm}$ .

## DISCUSSION

For "short pore" samples, all our observations are consistent with the porous layer behaving as independent pores. Depending on the diameter of the alumina constrictions at the pore mouth, and depending on the temperature, evaporation in a pore may occur either through the recession of the meniscus or by homogeneous cavit-



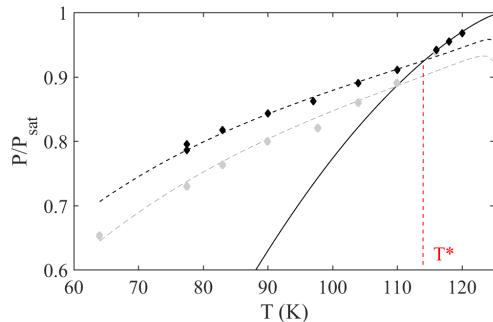


FIG. 9. Temperature dependence of the normalized evaporation pressure for the *same* PoSi sample as in Fig. 6, but prior to alumina deposition. Black symbols correspond to the evaporation pressure for the native state and grey ones to the evaporation pressure for reduced pore mouth. As in Fig. 6, the solid line is the CNT prediction for an energy barrier of  $46 k_B T$  and the dashed line is the equilibrium pressure in an aperture of diameter 10.9 nm.

tion.

For "long pore" samples and above a crossover temperature  $T^*$  which is sample dependent, we also observe cavitation. This was expected for samples with alumina deposit: above  $T^*$ , the alumina constrictions at the pore mouth are narrow enough to block the menisci and preclude evaporation from the sample surface. Thus, the liquid can reach the metastability limit for bulk cavitation in the whole volume, independently of the topology of the pore network. The fact that cavitation is also observed in *native* samples is more surprising. The simplest interpretation is that pores are not straight and that native constrictions in the pores play the same role as alumina constrictions at the aperture, *i.e.* control the recession of the meniscus below  $T^*$ . The existence of constrictions distributed along the pores is also suggested by NMR measurements of the diffusion constant along the pore axis [16, 17], and by permeability measurements [16], the values of both quantities being much smaller than expected for straight pores.

In this interpretation,  $D_{\text{eff}}$  is a typical diameter of these constrictions. This is supported by the value of the alumina thickness  $t_{\text{ob}}$  which is required to obstruct the pores. Assuming that constrictions exist close to the pore aperture, one expects  $D_{\text{eff}} \sim 2t_{\text{ob}}$ . This relationship is consistent with our measurements of  $D_{\text{eff}}$  and estimation of  $t_{\text{ob}}$  (see Supporting Information). Values of effective diameters for different porosities are gathered in Table II.

Turning now to evaporation below  $T^*$ , we find that native and ink-bottles samples exhibit different evaporation mechanisms. For native samples, we do not observe long-range correlation between pores. It is thus likely that meniscus recession occurs independently in each pore and

is controlled by the disorder induced by the constrictions. Then, each pore behaves as a one-dimensional disordered system, as proposed in Refs. [20, 34] to account for the H2 shape of isotherms. Discussing the shape of the isotherms and relating precisely the value of  $D_{\text{eff}}$  to the pore geometry would require to characterize the disorder along the pores and to take into account the distribution of pore diameters. This is well beyond the scope of the present work.

porosity	$\langle d \rangle$ (nm)	$D_{\text{eff}}$ (nm)	$T^*$ (K)	$d_{\text{eff}}$ (nm)
50 %	13	6.2	97	-
70 %	26	10.9	114	9
85 %	50	18	121	12

TABLE II. Average pore diameter  $\langle d \rangle$  (after [8]), effective diameter  $D_{\text{eff}}$  of constrictions along pores and effective diameter  $d_{\text{eff}}$  for connections between pores for several porosities, obtained from the evaporation pressure. We also give the crossover temperature  $T^*$  between meniscus recession and cavitation for native samples. For 50% porosity, only native samples were studied so that  $d_{\text{eff}}$  could not be determined. For 85% porosity, measurements were only performed at 77 K, and  $T^*$  is the estimated intercept of the cavitation curve and of the equilibrium curve for  $D_{\text{eff}} = 18$  nm.

Finally, coming to the evaporation mechanism for "long pore" ink-bottles below  $T^*$ , the very steep evaporation event observed in this case has specific features. First, the evaporation pressure is almost independent of the reduction of the pore mouth. This was demonstrated for hexane at room temperature [7]. We have checked that this holds for nitrogen at 77 K. As shown in Fig. 10 for a 85% porosity sample, we find that evaporation occurs at  $P_p \simeq 0.8P_{\text{sat}}$  whatever the alumina thickness, up to a value where the whole porous volume is almost completely disconnected from the vapor reservoir. Similar results were previously interpreted as a proof for cavitation [7, 9], which could only be heterogeneous since the homogeneous cavitation would occur close to  $0.5P_{\text{sat}}$ , well below  $P_p$ . This hypothesis is now ruled out: despite being a perfectly wetting fluid, helium indeed behaves as nitrogen, excluding the heterogeneous cavitation scenario.

The second feature is the long-range correlations between pores. While the simplest explanation is the existence of connections between neighbouring pores, another possibility, put forward by Grosman and Ortega [35], would be an indirect mechanical coupling. However, in view of our recent experiments on strain- and stress-induced adsorption [19], this mechanical coupling is negligible. Moreover, the existence of connections between pores is also suggested by the moderate anisotropy of the diffusion constant measured by NMR [16, 17]. All together, this makes the first explanation the most likely.

The third and last feature is the temperature depen-

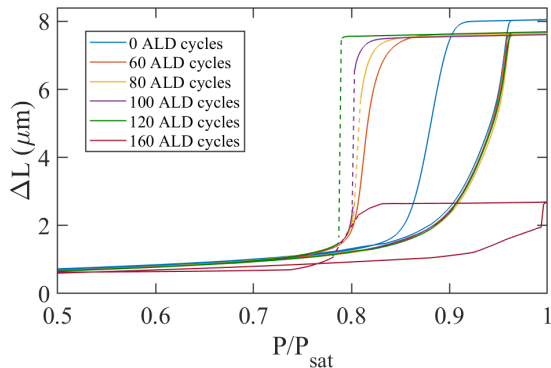


FIG. 10. Effect of successive alumina deposition on nitrogen isotherms at 77.4 K for a 85% porosity sample ( $\langle d \rangle = 50$  nm,  $l = 20 \mu\text{m}$ ). Whatever the alumina thickness, hence the pore aperture reduction, the steep evaporation step occurs at  $P_V/P_{\text{sat}} \simeq 0.8$ , corresponding to an effective diameter  $d_{\text{eff}} = 12$  nm. For 160 ALD cycles, the extent in  $L$  of the hysteresis loop is much reduced, implying that most of the pores are obstructed.

dence of the evaporation pressure, which is found to be the same as that for a meniscus receding through an aperture of effective diameter  $d_{\text{eff}}$ , smaller than the typical constriction size  $D_{\text{eff}}$ . As  $d_{\text{eff}}$  is independent on the fluid and on the thickness of the alumina coating, it has to be a characteristic dimension of the porous material, most probably related to connections between pores.

Bringing all these results together leads to the following scenario for long pores samples of porosities 70% and 85%. Without alumina deposit, the fluid evaporates mainly along the pores as the constrictions are, on average, wider than the connections between pores. The existence of connections has no impact on the evaporation mechanism. In contrast, when the pore mouths (or the constrictions close to the mouth) are reduced by alumina deposition, only the largest pores or defects in the pore network still present a mouth wider than the interconnections. It then becomes more favorable for the menisci to recede first in these largest pores, then through interconnections to finally reach the narrower pores. The observed long-range correlation during evaporation shows that this process is a collective one. By analogy with 3D disordered porous materials, we suggest that it involves a percolation phenomenon. Assuming that all constrictions within a pore are wider than the interconnections, a given pore will totally empty as soon as one of the neighboring pores to which it is connected will itself empty. The random nature of interconnections then gives rise to an invasion percolation phenomenon, the largest pores acting as germs. Because the underlying sites are the pores themselves, this percolation is likely 2D rather than 3D. Predicting the corresponding evaporation threshold (that is the value of  $d_{\text{eff}}$ ) would require

a detailed knowledge of the network topology, which is well beyond our current capability. However, we stress that this scenario provides a natural explanation to the dependence of  $d_{\text{eff}}$  on the details of the pore geometry, a feature which was difficult to explain in the hypothesis of heterogeneous cavitation. For instance, as shown in Fig. 1, the evaporation pressure increases with the pore length  $l$ . This can be explained by an increase in the diameter of the interconnections with the etching time, a reasonable hypothesis in view of an earlier work where we observed that the isotherms change with the etching time [19].

In this picture, the observation in the same samples of a small cavitation event (about 1 % of the total volume for the  $20 \mu\text{m}/70\%$  sample at 77 K) implies that some pores or some sections of the pores are connected to their neighbours only through some very narrow constrictions.

To summarize, the features of evaporation from "long pores" samples are consistent with porous silicon being a disordered and interconnected 3D pore network –with some anisotropy– rather than an array of straight independent pores. Actually, very few experiments point to the opposite conclusion. The crucial one [15], which initially promoted the model of independent pores, is an experiment performed using a 1-cm-size sample prepared in the same way and with a similar geometry as the present "long pore" samples (pore length about  $20 \mu\text{m}$  and porous layer still attached to the underlying wafer). When the sample was half covered with a thick aluminum layer – totally blocking the pores below the deposit – and subsequently exposed to an oxygen atmosphere, oxygen did not enter the pores below the Al layer, which was interpreted as a proof that pores are non interconnected. However, a major difference between this experiment and ours is the typical length scale at which communication between pores is tested. In the earlier experiment, no oxygen was detected in the pores a few mm away from the Al boundary. In contrast, present optical experiments reveal connections up to the  $\mu\text{m}$  scale. A precise modeling of the oxygen flow at large scale in a realistic pore network is then necessary to check whether the two observations may be reconciled or not.

## CONCLUSION

We have shown that evaporation in porous silicon membranes occurs either through homogeneous cavitation or by meniscus recession. In the latter case, pore-blocking can trigger a local or collective evaporation process. This variety of evaporation mechanisms is not consistent with a description of porous silicon as an array of independent straight pores aligned along the etching direction. This is in agreement with recent measurements of diffusion constant, permeability, elastic moduli

as well as images obtained by X-ray tomography. One of the major outcomes of the present work is a consistent picture, for all samples and all temperatures, of how the evaporation process is impacted by the defects of the pore array, these defects being schematically described as constrictions along the pore axis and interconnections between pores.

In this picture, the existence of interconnections is responsible for the spectacular long-range nature of evaporation, consistent with a percolation process, observed at low temperature for the long pores samples with reduced pore mouth. Such a behavior, which was previously misinterpreted as heterogeneous cavitation, is however restricted to those particular samples. In all other situations, and particularly for native samples, interconnections have no impact on the evaporation process, which occurs either through meniscus recession along the pore direction, or by cavitation. This reflects the fact that, on average, constrictions are larger than interconnections. Hence, the resulting structure of porous silicon and the evaporation process are highly anisotropic (as are elastic moduli, diffusion constants...).

The second important result is that, for long pore samples, we always observe a crossover between meniscus recession at low temperature and homogeneous cavitation at high temperature. The crossover temperature is controlled by the typical diameter of the constrictions for native samples or by that of the interconnections for samples with alumina deposition. Such a crossover is similar to the one observed in ordered cage-like porous silicas [4] whose behavior is now well understood [36]. For these systems, constrictions and interconnections are identical and monodisperse, so that  $d_{\text{eff}}=D_{\text{eff}}$  inferred from the evaporation pressure can be compared to their determination from structural studies. This contrasts with the case of Vycor, a prototype of tridimensional disordered porous material. Although a similar crossover between percolation and cavitation has been previously demonstrated for this material [13, 14], a direct comparison between  $d_{\text{eff}}$  and its complex structure seems out of reach. In other words, unlike in ordered cage-like porous silica,  $T^*$  cannot be precisely predicted from the material structure. The situation for porous silicon is similar. Nevertheless, we can safely expect that, as long as the pore network does not consist in an array of non-interconnected straight pores, cavitation should be the dominant evaporation process at high enough temperature.

Ultimately, the simplest situation is the one of short pore samples with alumina deposit, which can be considered as a array of independent pores. The fraction of such pores emptying through homogeneous cavitation depends on the pore aperture distribution and on the temperature. Since a strong reduction of the pore mouth allows to observe cavitation in a wide temperature range, such samples are powerful tools for studying

homogeneous cavitation. Moreover, as a single sample consists in  $10^{11}$  independant pores, it is straightforward to determine the cavitation rate, as demonstrated in porous alumina [7]. Compared to porous alumina, porous silicon layers are simpler to synthesize and have better optical properties as the surfaces have a better flatness. The wide pore size distribution is not an obstacle for studying homogeneous cavitation as long as the diameter of the critical nucleus is much smaller than the mean transverse pore size, a condition which is met for 85% porosity sample except in the very close vicinity of the bulk critical point. Experiments are currently in progress with the aim to obtain a more precise understanding why, as seen in Fig. 2, the cavitation pressure is shifted with respect to the CNT prediction at low temperature.

## SUPPORTING INFORMATION

Calibration of ALD deposition. Additional details on the determination of optical and volumetric isotherms for nitrogen and helium. Additional experimental data for native porous silicon samples. Determination of the helium cavitation pressure from volumetric isotherms.

## ACKNOWLEDGMENTS

We thank J. Puibasset for stimulating discussions, I. Vickridge for careful reading of the manuscript, the INSP workshop for designing the high pressure cell for the volumetric nitrogen experiment, the LPENS workshop for designing and building the entire high-pressure low-temperature optical setup, and the NEEL workshops for designing and machining parts of the helium set-up. This work, including the funding of M. B and F. S., has been financially supported by Agence Nationale de la Recherche through the project CavConf, ANR-17-CE30-0002.

## REFERENCES

- 
- \* rolley@phys.ens.fr, ORCID 0000-0003-1333-2541
- [1] Ravikovitch, P.; Neimark, A. Experimental confirmation of different mechanisms of evaporation from ink-bottle type pores: Equilibrium, pore blocking, and cavitation. *Langmuir* **2002**, *18*, 9830–9837.
  - [2] Vishnyakov, A.; Neimark, A. V. Monte Carlo Simulation Test of Pore Blocking Effects. *Langmuir* **2003**, *19*, 3240–3247.
  - [3] Morishige, K.; Tateishi, N. Adsorption hysteresis in ink-bottle pore. *J. Chem. Phys.* **2003**, *119*, 2301–2306.

- [4] Morishige, K.; Tateishi, M.; Hirose, F.; Aramaki, K. Change in Desorption Mechanism from Pore Blocking to Cavitation with Temperature for Nitrogen in Ordered Silica with Cagelike Pores. *Langmuir* **2006**, *22*, 9220–9224, PMID: 17042533.
- [5] Rasmussen, C. J.; Vishnyakov, A.; Thommes, M.; Smarsly, B. M.; Kleitz, F.; Neimark, A. V. Cavitation in Metastable Liquid Nitrogen Confined to Nanoscale Pores. *Langmuir* **2010**, *26*, 10147–10157, PMID: 20210340.
- [6] Blander, M.; Katz, J. L. Bubble nucleation in liquids. *AIChE Journal* **1975**, *21*, 833–848.
- [7] Doebele, V.; Benoit-Gonin, A.; Souris, F.; Cagnon, L.; Spathis, P.; Wolf, P. E.; Grosman, A.; Bossert, M.; Trimaille, I.; Rolley, E. Direct Observation of Homogeneous Cavitation in Nanopores. *Phys. Rev. Lett.* **2020**, *125*, 255701.
- [8] Grosman, A.; Ortega, C. Capillary condensation in porous materials. Hysteresis and interaction mechanism without pore blocking/percolation process. *Langmuir* **2008**, *24*, 3977–3986.
- [9] Grosman, A.; Ortega, C. Cavitation in Metastable Fluids Confined to Linear Mesopores. *Langmuir* **2011**, *27*, 2364–2374.
- [10] Mason, G.; Everett, D. H. A model of adsorption-desorption hysteresis in which hysteresis is primarily developed by the interconnections in a network of pores. *Proceedings of the Royal Society of London. A. Mathematical and Physical Sciences* **1983**, *390*, 47–72.
- [11] Page, J. H.; Liu, J.; Abeles, B.; Herbolzheimer, E.; Deckman, H. W.; Weitz, D. A. Adsorption and desorption of a wetting fluid in Vycor studied by acoustic and optical techniques. *Phys. Rev. E* **1995**, *52*, 2763–2777.
- [12] Soprunyuk, V. P.; Wallacher, D.; Huber, P.; Knorr, K.; Kityk, A. V. Freezing and melting of Ar in mesopores studied by optical transmission. *Physical Review B* **2003**, *67*, 144105.
- [13] Bonnet, F.; Melich, M.; Puech, L.; Wolf, P. E. Light scattering study of collective effects during evaporation and condensation in a disordered porous material. *Europhys. Lett.* **2013**, *101*, 16010.
- [14] Bonnet, F.; Melich, M.; Puech, L.; Anglès d’Auriac, J.-C.; Wolf, P.-E. On Condensation and Evaporation Mechanisms in Disordered Porous Materials. *Langmuir* **2019**, *35*, 5140–5150, PMID: 30865460.
- [15] Coasne, B.; Grosman, A.; Ortega, C.; Simon, M. Adsorption in Noninterconnected Pores Open at One or at Both Ends: A Reconsideration of the Origin of the Hysteresis Phenomenon. *Phys. Rev. Lett.* **2002**, *88*, 256102.
- [16] Puibasset, J.; Porion, P.; Grosman, A.; Rolley, E. Structure and Permeability of Porous Silicon Investigated by Self-Diffusion NMR Measurements of Ethanol and Heptane. *Oil & Gas Science and Technology—Revue d’IFP Energies nouvelles* **2016**, *71*, 54.
- [17] Kondrashova, D.; Lauerer, A.; Mehlhorn, D.; Jobic, H.; Feldhoff, A.; Thommes, M.; Chakraborty, D.; Gommès, C.; Zecevic, J.; De Jongh, P., et al. Scale-dependent diffusion anisotropy in nanoporous silicon. *Scientific reports* **2017**, *7*, 1–10.
- [18] Rolley, E.; Garroum, N.; Grosman, A. Using capillary forces to determine the elastic properties of mesoporous materials. *Phys. Rev. B* **2017**, *95*, 064106.
- [19] Bossert, M.; Grosman, A.; Trimaille, I.; Noûs, C.; Rolley, E. Stress or Strain Does Not Impact Sorption in Stiff Mesoporous Materials. *Langmuir* **2020**, *36*, 11054–11060.
- [20] Naumov, S.; Khokhlov, A.; Valiullin, R.; Kärger, J.; Monson, P. A. Understanding capillary condensation and hysteresis in porous silicon: Network effects within independent pores. *Physical Review E* **2008**, *78*, 060601.
- [21] Gor, G.; Huber, P.; Bernstein, N. Adsorption-induced deformation of nanoporous materials - A review. *Applied Physics Reviews* **2017**, *4*, 011303.
- [22] Grosman, A.; Puibasset, J.; Rolley, E. Adsorption-induced strain of a nanoscale silicon honeycomb. *EPL* **2015**, *109*, 56002.
- [23] Span, R.; Lemmon, E. W.; Jacobsen, R. T.; Wagner, W. A Reference Quality Equation of State for Nitrogen. *International Journal of Thermophysics* **1999**, *19*, 1121–1132.
- [24] Span, R.; Lemmon, E. W.; Jacobsen, R. T.; Wagner, W.; Yokozeki, A. A Reference Equation of State for the Thermodynamic Properties of Nitrogen for Temperatures from 63.151 to 1000 K and Pressures to 2200 MPa. *Journal of Physical and Chemical Reference Data* **2000**, *29*, 1361–1433.
- [25] Casanova, F.; Chiang, C. E.; Li, C.-P.; Roshchin, I. V.; Ruminski, A. M.; Sailor, M. J.; Schuller, I. K. Gas adsorption and capillary condensation in nanoporous alumina films. *Nanotechnology* **2008**, *19*, 315709.
- [26] Saam, W. F.; Cole, M. W. Excitations and thermodynamics for liquid-helium films. *Phys. Rev. B* **1975**, *11*, 1086–1105.
- [27] Cheng, E.; Cole, M. W. Retardation and many-body effects in multilayer-film adsorption. *Phys. Rev. B* **1988**, *38*, 987–995.
- [28] Tanaka, K. K.; Tanaka, H.; Angéilil, R.; Diemand, J. Simple improvements to classical bubble nucleation models. *Phys. Rev. E* **2015**, *92*, 022401.
- [29] Baidakov, V.; Vinogradov, V.; Pavlov, P. Homogeneous nucleation in liquid nitrogen at negative pressures. *J. Exp. Theor. Phys.* **2016**, *123*, 629–637.
- [30] Maris, H. J.; Xiong, Q. Nucleation of bubbles in liquid helium at negative pressure. *Phys. Rev. Lett.* **1989**, *63*, 1078–1081.
- [31] Arvengas, A.; Herbert, E.; Cersoy, S.; Davitt, K.; Caupin, F. Cavitation in heavy water and other liquids. *The Journal of Physical Chemistry B* **2011**, *115*, 14240–14245.
- [32] Bruot, N.; Caupin, F. Curvature dependence of the liquid-vapor surface tension beyond the Tolman approximation. *Physical review letters* **2016**, *116*, 056102.
- [33] Azouzi, M. E. M.; Ramboz, C.; Lenain, J.-F.; Caupin, F. A coherent picture of water at extreme negative pressure. *Nature Physics* **2013**, *9*, 38–41.
- [34] Puibasset, J. Adsorption-desorption hysteresis of simple fluids confined in realistic heterogeneous silica mesopores of micrometric length: A new analysis exploiting a multi-scale Monte Carlo approach. *J. Chem. Phys.* **2007**, *127*, 154701.
- [35] Grosman, A.; Ortega, C. Influence of elastic strains on the adsorption process in porous materials: an experimental approach. *Langmuir* **2009**, *25*, 8083–8093.
- [36] Morishige, K. Revisiting the Nature of Adsorption and Desorption Branches: Temperature Dependence of Adsorption Hysteresis in Ordered Mesoporous Silica. *ACS Omega* **2021**, *6*, 15964–15974.

